On the effect of boat-tails on a simplified heavy vehicle geometry under crosswinds

On the Effect of Boat-tails on a Simplified Heavy Vehicle Geometry under Crosswinds

Mohab Hassaan, Divyang Badlani, Mehdi Nazarinia*

School of Engineering and Physical Sciences, Heriot-Watt University, Edinburgh, United Kingdom

Abstract

The flow around a Ground Transport System (GTS), is numerically investigated using steady RANS model; $k-\omega$ SST, at a Reynolds number of $\sim 2\times10^6$. This paper focuses on the effect of crosswinds on the near-wake structure of the GTS with and without boat-tails. Upon the emanation of crosswinds, a quadratic increase in the drag coefficient (C_D) was observed, as a function of the yaw angle. Such an increase is attributed to the break in the symmetry of near-wake structure and three, streamwise vortices emanating from the leading edges of the GTS. Boat-tail with a slant angle of 15°, at zero yaw, has resulted in a (C_D) reduction of up to $\sim$ 50%, relative to the baseline GTS. The reduction is consistent with previous studies on various simplified geometries. Such reduction is a resultant of a smaller wake length, coupled with an overall increase in the pressure in the wake, consequently increasing the mean base pressure coefficient. Higher boat-tail angles have resulted in an increase in CD, whereas, under crosswind, $\sim$ 40% reduction in (C_D) is observed. Boat-tails have additionally resulted in a quasi-symmetric near-wake structure, under crosswinds, acting as a blockage and preventing the interaction between the three streamwise vortices and the near-wake.

Keywords: Ground Transportation System (GTS), boat-tail, near-wake, crosswinds, Computational Fluid Dynamics (CFD), flow topology

1. Introduction

In the automotive industry, reduction in the aerodynamic drag encountered by heavy vehicles poses as an ongoing challenge for heavy vehicle manufacturers. The significance of aerodynamic drag arises past a freestream velocity of $\sim$ 80 km hr^{-1}, at which aerodynamic drag becomes the dominant resistive force of a typical heavy vehicle (Söderblom et al., 2016). Such significance is a resultant of its quadratic increase relative to the freestream velocity, with earlier studies showing aerodynamic drag to be responsible for $\sim$ 60% of the total fuel consumption of an average heavy vehicle at typical highway velocities ($\sim$ 100 km hr^{-1}) (McCallen et al., 1999; Lögdberg, 2008).

Aerodynamically speaking, the geometry of a heavy vehicle is regarded as a *bluff body*. Around a heavy vehicle, an estimated 25% of the total aerodynamic drag arises from the rear-end of the body (Wood, 2006). Here, the *bluffness* of the body triggers a low pressure, separation bubble downstream, denoted to as the *wake region* (Grandemange et al., 2013). The aerodynamic drag experienced by a *bluff body* is directly related to the wake structure and dynamics (Corallo et al., 2015).

Appropriate drag reduction devices have the potential to reduce the drag coefficient of a typical heavy vehicle by $\sim$ 50% (McCallen et al., 1999). Generally, drag reduction devices can be categorized into *active devices*, *i.e.* devices that utilize external energy to influence the flow around a vehicle (Howell et al., 2003), and *passive devices*, *i.e.* geometric alterations used to regulate the flow around a vehicle and therefore reducing its drag coefficient (Choi et al., 2014).

A boat-tail is a passive add-on device comprising four plates, each attached to the trailing edge of the trailer, as seen in figure 1. The boat-tail angle (α in figure 1) represents the inclination of the plates with respect to the edge perpendicular to the base surface. The device is aimed at delaying separation at the vehicle's trailing edge by altering the angle of flow inwards and consequently reducing the size of the wake.

Early research on boat-tails has shown its potential in reducing aerodynamic drag (Cooper, 1985; Croll et al., 1995; Gutierrez et al., 1996; Coon and Visser, 2004). Such drag reduction is highly dependent on the boat-tail

*Corresponding author
Email address: m.nazarinia@hw.ac.uk (Mehdi Nazarinia)

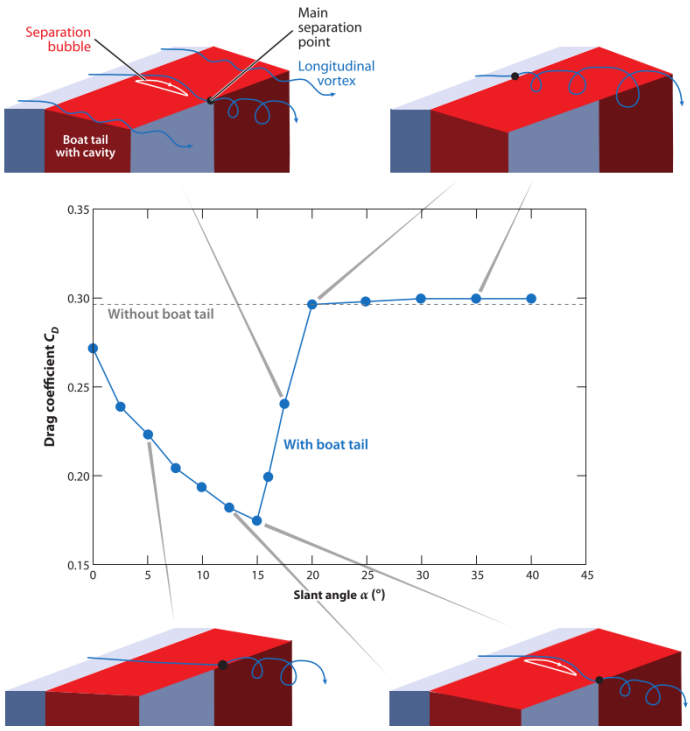

Figure 1: Variation of the drag coefficient (C_D) with the inclination boat-tail angle (α) on the General Motors (GM) simplified geometry. The horizontal dotted line corresponds to C_D of the baseline body (*i.e.* without boat-tail). The sub-figure at each corner demonstrates the flow field within proximity to the upper boat-tail plate along the vertical symmetry plane, for various inclination angles. Figure taken from Yi et al. (2007).

angle, with studies reporting up to $\simeq 50\%$ drag reduction at a boat-tail angle of 15° on the General Motors (GM) model (Yi et al., 2007), and a simplified truck model with no tractor/trailer gap (Burton et al., 2011). Both studies have additionally shown an abrupt rise in drag for higher boat-tail angles (refer to figure 1).

Generally, the overall structure of the wake region is difficult to predict, as it has been shown to be a function of various flow and geometric parameters (Badlani, 2018; Hassaan, 2018; Corallo et al., 2015; McArthur et al., 2016). The complexity of the flow around bluff bodies has led to the establishment of various simplified geometries, each designed to mimic and study the flow around a specific type of vehicle (Good and Garry, 2004). The Ground Transportation System (GTS) is a simplified geometry designed by Sandia National Laboratories to study the flow in the *near-wake region* of a heavy vehicle, *i.e.* the region in the wake prior to the converging streamlines downstream of a body. The GTS is characterized by an elliptical front-end and an aspect ratio of 1.39, designed to ensure a continuously attached flow over the top surface of the body. Key dimensions of the full scale GTS can be found in Croll et al. (1995). For simplicity, cylindrical struts have been attached to the bottom surface of the GTS replacing conventional wheel geometries (Gutierrez et al., 1996).

The aerodynamic drag associated with the GTS has been shown to be a function of various geometric and flow parameters. Initially, Storms et al. (2001) experimentally showed a $\sim 40\%$ variation in the GTS aerodynamic drag (C_D) within the laminar and transition Reynolds numbers ($3 \times 10^5 \leq Re_w \leq 1 \times 10^6$). Such variation was numerically matched by Badlani (2018) and Hassaan (2018), where the variation in C_D was correlated to a change in the feeding mechanism, *i.e.* the vertical direction of the flow within the near-wake. The near-wake of the GTS, at the vertical symmetry plane, for laminar Re_w is characterized by a lower, larger vortex feeding the flow onto a relatively smaller, upper vortex (upward feeding) (McArthur et al., 2016). An inverse in the feeding mechanism in the turbulent Re_w range results in a distinct near-wake structure relative to laminar Re_w. Here, the near-wake topology is characterized by an upper (now larger) vortex feeding the flow onto a lower vortex (Roy and Ghuge, 2009; Maddox et al., 2004).

Another flow variable that has been shown to affect the flow structure proximate to ground vehicles is the magnitude and direction of crosswinds (Rao et al., 2018). While visualization of the near-wake structure of a vehicle with the absence of crosswinds is important in the design process of novel drag reduction devices, varying magnitude and direction of crosswinds can significantly alter a vehicle's stability (Cheli et al., 2006). Heavy vehicles are specifically more sensitive to the variation of crosswinds relative to other ground vehicles (McArthur et al., 2018).

Such sensitivity is a resultant of their notably higher side areas, increasing the magnitude of side forces experienced by a typical heavy vehicle, and consequently increasing its rollover coefficient.

Wind fences have also been previously studied, for their potential in reducing the rollover coefficient of trucks in the presence of crosswinds. Alonso-Estébanez et al. (2017) analyzed the effect of wind fence geometries on the aerodynamics of a truck using the $SSTk--\omega$ formulation under crosswind conditions. Here, higher fences coupled with increased fence and truck distance were shown to aid in the reduction of the rollover coefficient.

Earlier studies conducted on the GTS have shown the emanation of two, co-rotating, streamwise vortices from the corners of the upper leading edge upon the induction of crosswinds (Croll et al., 1995). Particle Image Velocimetry (PIV) conducted within the same study show both the streamwise vortices to develop downstream onto the near-wake. Pressure measurements experimentally obtained by McArthur et al. (2018) in the near-wake of a scaled heavy vehicle model show low pressure regions corresponding to both the streamwise vortices observed by Croll et al. (1995) on the GTS, suggesting crosswinds to have a similar effect on the GTS and typical heavy vehicle geometries.

Along the mid-height plane, in the near-wake of the GTS, in the absence of crosswinds, the flow structure comprises two, counter-rotating vortices of equal size, converging onto a saddle point downstream (Salari et al., 2004; McArthur et al., 2016; Badlani, 2018; Hassaan, 2018). A break in such horizontal symmetry was shown upon the induction of crosswinds, indicated by the variation of the size of each of the counter-rotating vortices in the near-wake, and the horizontal shift of the stagnation point along the base of the GTS (Van Raemdonck, 2012; Storms et al., 2001). It should be noted that studies, such as McArthur et al. (2018), have suggested that numerical simulations conducted using steady *Reynolds Averaged Navier Stokes* (RANS) turbulence models are unable to replicate such asymmetric near-wake structures. However, as presented within the current study, appropriate mesh refinement results in capturing such asymmetry (see sections 3 and 4).

The present study investigates the effect of a boat-tail on the near-wake topology of the GTS under the effect of crosswinds. Initially, the effect of crosswinds on the wake structure of the GTS, prior to the implementation of a boat-tail, is reported. It is followed by the effect of implementing a boat-tail at a varying slant angle with and without crosswinds. The remainder of the paper is organized as follows; section 2 presents details of the numerical setup used within the study, section 3 reports the conducted validation study, while the results of the study are presented in section 4.

2. Numerical Setup

Throughout the present study, the $1:8$ scaled GTS is used to numerically investigate the effect of a boat-tail's slant angle on the coefficient of drag and the correlated effects on the near-wake topology. The geometry used within the study is identical to the one introduced by Storms et al. (2001), with four cylindrical stilts, attached to the bottom surface of the GTS. The outer diameter of each of the stilts ($D^* = D/w$, $w = GTS\ width$) equates to 0.12. The dimensions of the $1:8$ scaled GTS are presented in figure 2 in meters.

The full numerical domain used within the study is of total length, width and height of 7, 4 and 1.6 GTS lengths, respectively. The blockage ratio associated with the numerical domain, *i.e.* the ratio of the frontal area of the GTS relative to the frontal area of the numerical domain, equates to $\sim 0.4\%$. Further decreasing the blockage ratio was found to have no effect on the aerodynamic forces of the GTS and therefore the solution was considered *domain size independent*. The GTS was placed 1.5 and 4.5 truck lengths away from the headwind inlet and headwind outlet (refer to figure 2), at a normalized height from the ground ($G^* = G/w$) equating to 0.24. An identical ground clearance was used previously by Storms et al. (2001); Roy and Ghuge (2009); Salari et al. (2004); Badlani (2018).

The coordinate system origin is positioned on the vertical symmetry plane at the bottom trailing edge of the GTS. Here, the X axis is parallel to the longitudinal axis of the GTS, the Z axis is parallel to the height of the geometry and points vertically upwards, and the Y axis follows the conventional cartesian system, as can be seen in figure 2. Unless and otherwise stated, the coordinates and all the dimensionless numbers were normalized by the width of the GTS ($[X^*, Y^*, Z^*] = [X, Y, Z]/w$), following the convention of Storms et al. (2001).

Figure 3 shows a schematic of the geometry of GTS with boat-tail. Four boat-tail plates, with a normalized thickness of ~ 0.01, were attached to the trailing edges of the GTS. Following the convention of Burton et al. (2011), the angle β represents the inclination angle of the boat-tail, while B^* is the ratio of the boat-tail's horizontal length (B) and the hydraulic diameter (D_H) of the GTS. It should be noted that the boat-tail angle used within the present study (β), is similar to the slant angle (α) used in figure 1 by Yi et al. (2007). The hydraulic diameter is defined as;

$$D_H = \sqrt{\frac{4A_c}{\pi}} \tag{1}$$

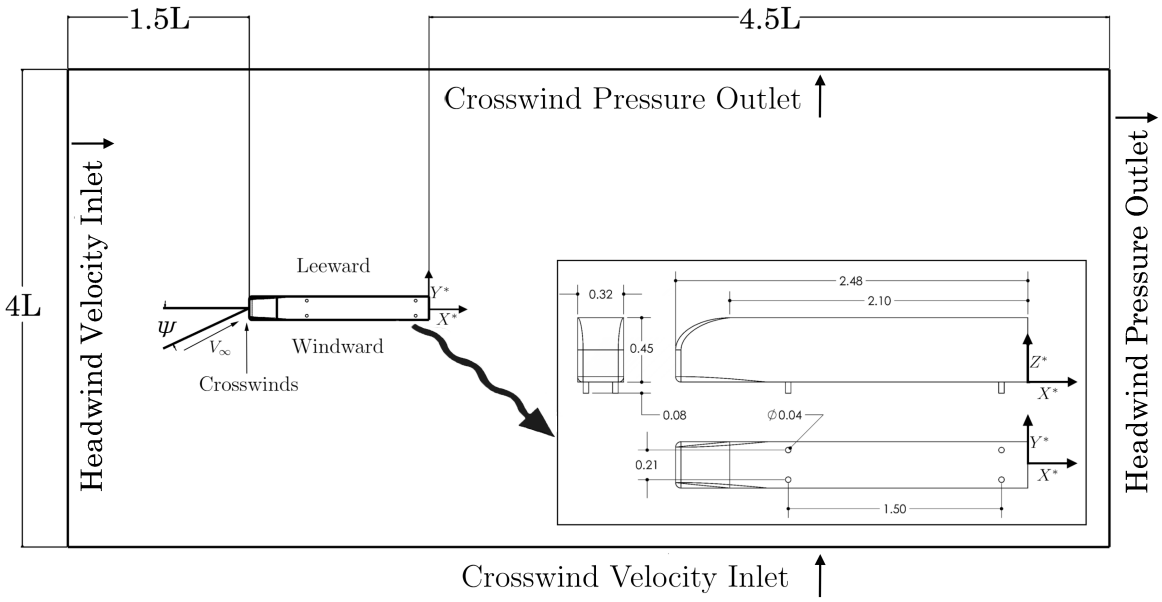

Figure 2: Top view of the numerical domain used within the present study. Here, L denotes the length of the $1:8$ GTS, ψ is the yaw angle and V_∞ is the freestream velocity. Locations of the headwind and crosswind inlets and outlets are labelled in their respective locations. The *windward* and *leeward* sides of the numerical domain represent positive and negative Y^* axis coordinates, respectively. The subfigure at the bottom right is a schematic of the $1:8$ scaled GTS, shown in front (top left), side (top) and top (bottom) views, along with key dimensions. Dimensions in the subfigure are in meters.

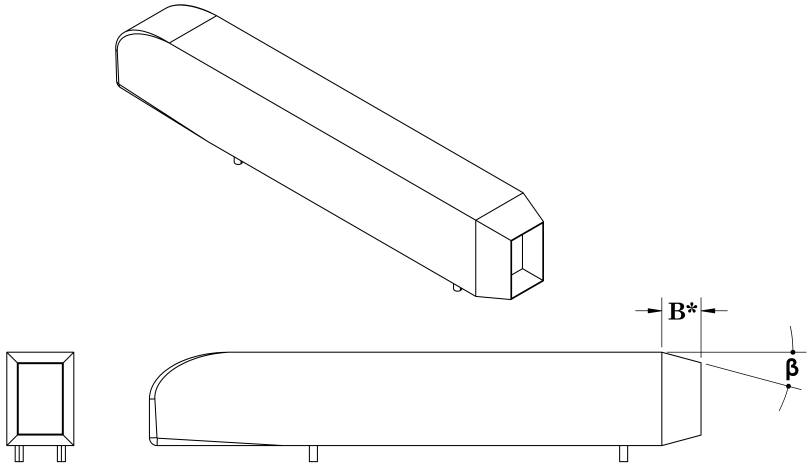

Figure 3: Schematic of the boat-tail plates attached to the GTS, shown in isomeric (top), rear (bottom left) and side (bottom right) views, where β and B^* are the boat-tail slant angle and normalized length (by the hydraulic diameter), respectively.

where A_c is the cross sectional area of the GTS (Burton et al., 2011). To distinguish between the GTS with and without boat-tail, the GTS prior to the attachment of the boat-tail will hereby be regarded as the *baseline GTS*.

Within the present study, a yaw angle (ψ) is defined as the angle at which the resultant of both the velocity components; the uniform velocity encountered by the vehicle, and crosswind, is directed relative to the longitudinal axis of the GTS (refer to figure 2). Here, a positive yaw angle represents a counter-clockwise rotation of the flow relative to the X axis, and the direction of crosswinds is parallel to the positive Y axis direction. It should be noted that following the convention of previous studies conducted on crosswinds, windward and leeward sides of the GTS represent the side facing the crosswind (upwind), and the side facing away from crosswind (downwind), respectively. In the present study, the definitions are additionally used to describe positive (leeward) and negative (windward) Y axis coordinates.

2.1. Numerical formulation

The numerical study was conducted using the Computational Fluid Dynamics (CFD) solver; ANSYS FLUENT^{TM}. The steady formulation of the Reynolds Averaged Navier Stokes (RANS) equations were used to solve the flow. Turbulence was solved using the two-equation, $k-\omega$ *Shear Stress Transport* (SST) turbulence model (Menter, 1994); a hybrid between $k-\omega$ and $k-\epsilon$ turbulence models. The numerical formulation of the $k-\omega$ SST model can be found in Menter (1994).

The yaw angle was varied by varying both the velocity components; the crosswind velocity (u_z), as a function of the *headwind velocity i.e* the velocity encountered by the vehicle (u_x), as presented in equation (2). Throughout the present study, the Reynolds number (Re_w) (based on the headwind velocity) was kept at a constant value of ~ 2 million. Here, a constant velocity equating to 93.91 ms^{-1} was imposed onto the headwind inlet, while the velocity at the crosswind inlet varied with the variation of the yaw angle, using equation (2). A no-slip boundary condition was imposed on all surfaces of the GTS and the bottom of the numerical domain. The top surface of the domain was modelled as an inviscid wall (symmetry), while atmospheric pressure was imposed onto both the outlets.

$$u_z = u_x \times tan(\psi) \tag{2}$$

The *hybrid initialization* method was used to initialize the solution. Here, a turbulence intensity of 0.25% was imposed onto the flow, to match the properties of the wind tunnel experiments reported by Storms et al. (2001). Two criteria were considered in evaluating the convergence of the numerical models. Each model was deemed converged as the absolute residuals of the transport equation and mass flux fall below 1×10^{-5}, in addition to a drag coefficient variation lesser than 0.1% over 100 iterations.

Figure 4 presents side and top views of the mesh used within the study. The mesh is constructed entirely out of unstructured, tetrahedral cells, with exception to the surfaces of the GTS and the bottom of the numerical domain. Here, 15 layers of prism cells were imposed onto the surfaces, where the y^+ value of the GTS surfaces varied for each mesh case (refer to figure 5). A higher mesh resolution was used around the GTS, and in the wake region, as flow variation within the regions significantly vary the aerodynamic forces of the GTS.

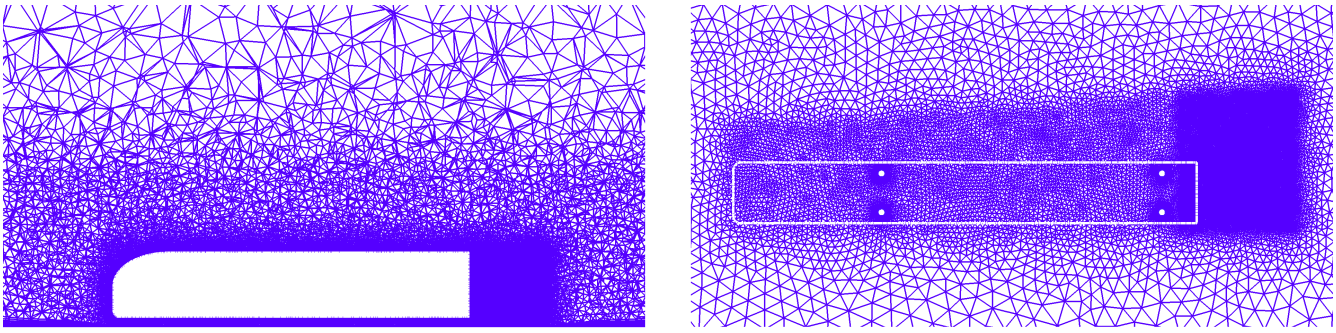

(a) Side view (b) Top view

Figure 4: An overview of the mesh used for the present study shown in (a) side view ($Y^* = 0$ plane), and (b) top view ($Z^* = 0.7$ plane). The white outline in subfigures (a) and (b) represent the outline the of the GTS.

The final mesh used for the study was concluded using a mesh dependency study, based on the GTS drag coefficient (C_D). Four mesh cases were considered within the study, with a total number of cells (n_{cell}) ranging from $\sim 1.2 \times 10^6$ to $\sim 7.5 \times 10^6$. Figure 5 shows the results of the mesh dependency study. A quadratic decline of C_D as a function of n_{cell} can be observed, with $\sim 1\%$ difference between mesh cases 3 (3.34×10^6), and 4 ($\sim 7.42 \times 10^6$). It is evident that the variation of C_D, as a function of n_{cell} is directly related to the variation of the mean y^+ value of the GTS surfaces ($\overline{y^+}$). Here, $\overline{y^+}$ exhibits a similar quadratic decline to C_D, relative to n_{cell}. It should be noted that absolute convergence is expected to occur at $\overline{y^+}$ lower than ~ 5.

3. Validation

To assess the numerical setup's validity under crosswinds ($\psi \neq 0°$), a comparison between the computed drag coefficient (C_D) within the present study ($Re_w = 2 \times 10^6$) and the numerical and experimental results of Salari et al. (2004) and Storms et al. (2001), is presented in figure 6 (a). It can be clearly seen that the drag coefficient computed by the three studies is within reasonable agreement, particularly between the present study and Storms

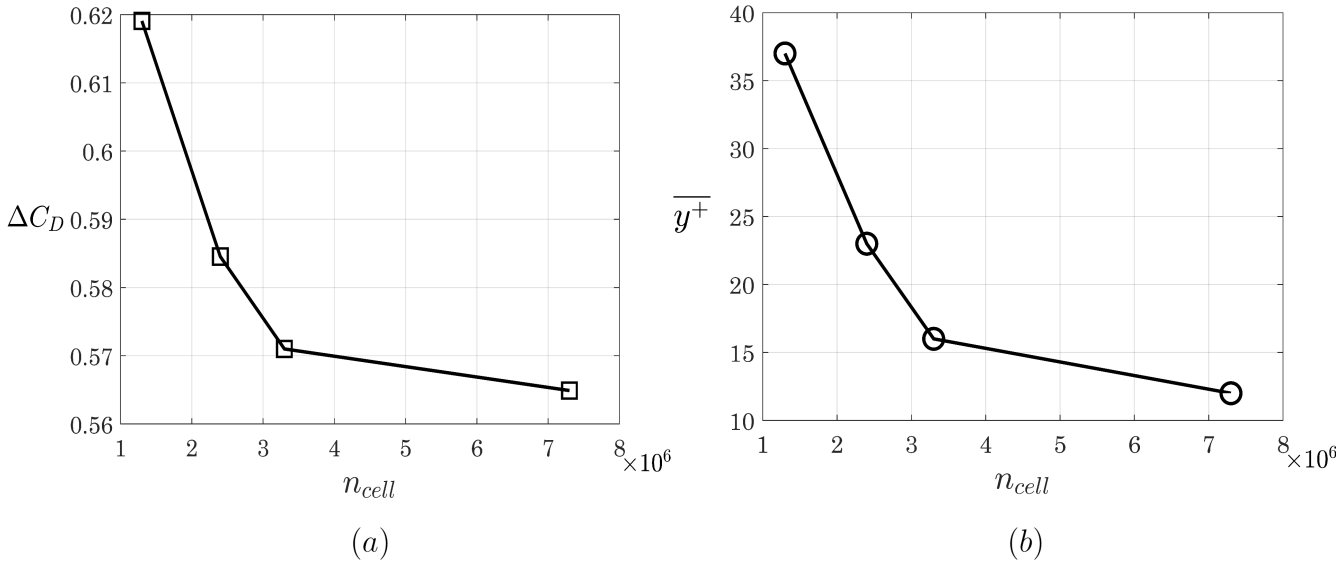

Figure 5: Mesh dependency study conducted between four mesh cases, where (a) is the variation of the GTS drag coefficient (C_D) as a function of the total number of cells (n_{cell}), and (b) is the variation of the mean y^+ of the GTS surfaces ($\overline{y^+}$) relative to n_{cell}.

et al. (2001), where the percentage difference between them is $\sim 1\%$. It is important to note that the total number of cells used within Salari et al. (2004) is $\sim 14 \times 10^6$, twice the number of cells used within the present study.

Additionally, the variation of C_D relative to ψ° is compared to Croll et al. (1995), who experimentally investigated the effect of ψ on the aerodynamic forces around the GTS embedded with wheel geometries at $Re_w = 1.6$ million. The comparison is presented in figure 6 (b). A quadratic increase of C_D relative to ψ can be observed within both studies. Here, a quasi-constant difference in C_D for $\psi < 8^\circ$ equating to $\simeq 0.04$ shows the effect of the wheel geometries on the drag coefficient. Such an effect is more notable for $\psi > 8^\circ$, where the difference between C_D associated with both studies equates to $\simeq 0.7$.

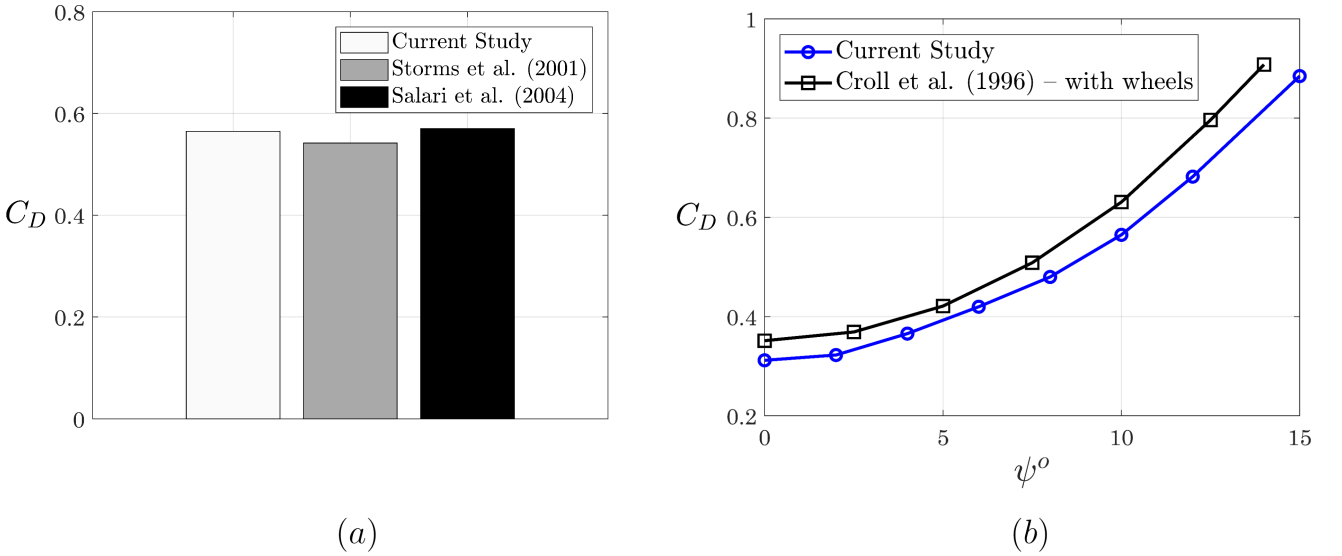

Figure 6: Comparison of the GTS drag coefficient (C_D) computed within the present study ($Re_w \sim 2$ million) (white) with the emanation of crosswinds, with; (a) the numerical and experimental work of Salari et al. (2004) ($Re_w = 2$ million) (black) and Storms et al. (2001) ($Re_w = 2$ million) (dark grey) for $\psi = 10^\circ$, and (b) the experimental work of Croll et al. (1995) ($Re_w = 1.6$ million) (black squares) for the yaw angle range; $0 \leq \psi^\circ \leq 15$.

Figure 7 shows a velocity vector field comparison between the present study and that experimentally obtained by Croll et al. (1995), along the $X^* = 1.39$ plane. Both studies show two recirculating regions along the top and

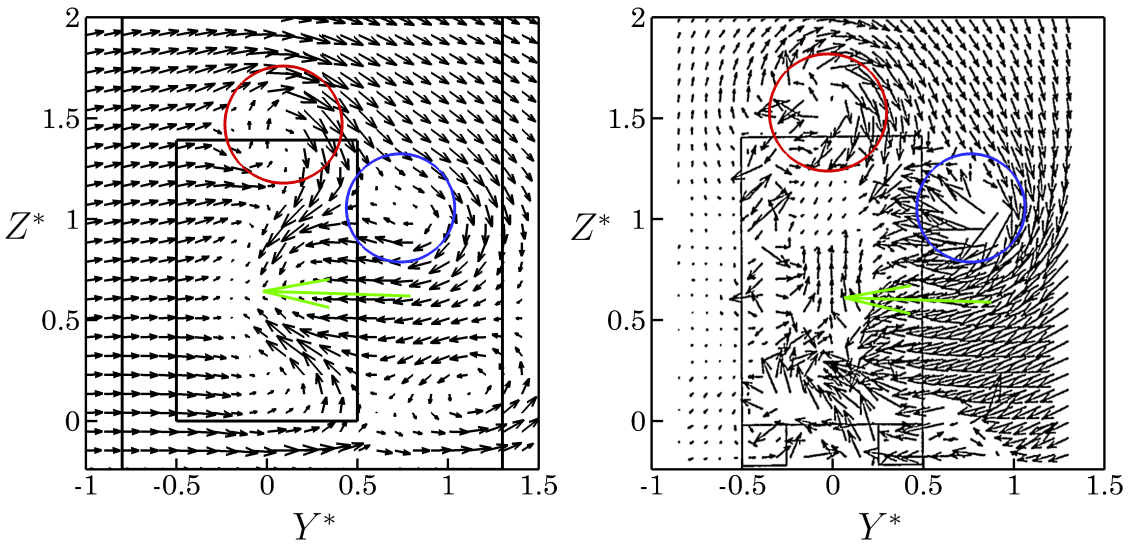

Figure 7: A comparison between the velocity vector field along the $X^* = 1.39$ plane between (a) the current study ($Re_w \sim 2$ million), (b) the experimental work Croll et al. (1995) ($Re_w = 1.6$ million). The large and small outlines in (a) correspond to the outline of the GTS and the figure presented in (b), respectively. The red and blue outlines in both the subfigures denote to the top and leeward recirculating regions, respectively. The green arrow in both the subfigures the flow structure along the centre of the base of the truck. The crosswind direction is from left to right in the two subfigures. Note: Only one in twelve vectors are shown for clarity.

leeward sides of the plane, albeit the upper recirculating region is closer to the leeward trailing edge. Furthermore, an additional recirculating region, at $[Y^*, Z^*] \simeq [1.16, 0.18]$ is computed within the present study. The recirculating region computed within the present study (leeward bottom side) was not observed in Croll et al. (1995). Such discrepancy is likely due to the wheel geometry's effect upstream, disrupting the development of the recirculating region.

4. Results

The effect of implementing a boat-tail at a varying boat-tail angle (β), on the 1 : 8 GTS is investigated for various yaw angles (ψ). Initially, the effect of varying ψ on the near-wake structure of the GTS is reported within the range; $0 \leq \psi^\circ \leq 15$. Previously, a similar yaw angle range ($0 \leq \psi^\circ \leq 14$) was suggested to be of importance in the automotive industry (Hucho and Sovran, 1993), hence the choice of the investigated range. The discussion is followed by section 4.1, where the effect of varying the boat-tail length (B^*) and slant angle (β) on the GTS drag coefficient (C_D) and the corresponding changes in the near-wake structure are discussed in for $\psi = 0^\circ$. Next, the effect of varying β on C_D and the near-wake structure of the GTS is reported for a varying yaw angle within the range; $0 \leq \psi^\circ \leq 10$ in section 4.2.

The study was conducted at $Re_w = 2.08 \times 10^6$. Studies such as Storms et al. (2001), Hassaan (2018) and Badlani (2018) on the GTS, have shown $Re_w = 2.08 \times 10^6$ to be within the turbulent Re_w range. Henceforth, the computed near-wake structure at $Re_w = 2.08 \times 10^6$ is expected to be similar to the GTS at highway Reynolds numbers.

Figure 8 (a) shows the variation of the baseline GTS drag coefficient (C_D) with the increase of ψ, relative to C_D at $\psi = 0^\circ$ (no crosswinds) ($\Delta C_D, \Delta C_D = C_D - C_{D_{\psi=0^\circ}}$). Here, a quadratic increase in C_D relative to ψ can be observed, where $\sim 180\%$ rise in C_D is computed for $\psi = 15^\circ$, relative to $\psi = 0^\circ$. Such quadratic rise in C_D is related to the change in the mean base pressure coefficient (ΔC_{p_b}), where a corresponding quadratic decline is computed relative to ψ, as can be seen in figure 8 (b). Flow visualization of the investigated yaw angle range conclude three distinct near-wake structures around the baseline GTS, corresponding to $0 \leq \psi^\circ \leq 2$, $2 < \psi^\circ \leq 8$ and $8 < \psi^\circ \leq 15$. The quadratic decline in C_{p_b} is a resultant of the change in the near-wake structure, as demonstrated within the remainder of the section.

To visualize vortical structures proximate to the baseline GTS, the λ_2 criterion, a Galilean-invariant method ($\lambda_2 = -1500$) is calculated for $\psi = 0^\circ$, 8° and 15°. Details of the formulation associated with the criterion can be found in Jeong and Hussain (1995).

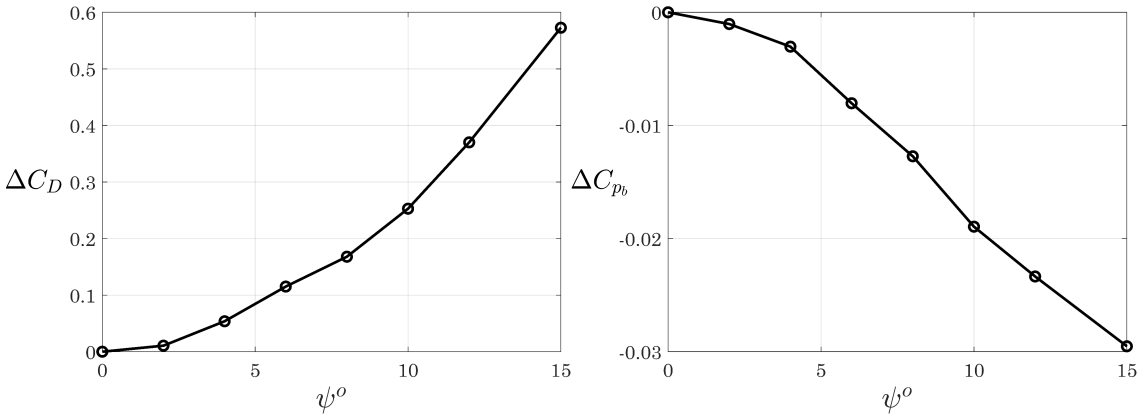

(a) Changes of drag coefficient

(b) Changes of pressure coefficient

Figure 8: Variation of the change in the baseline GTS (no boat-tail) drag coefficient ΔC_D (shown in subfigure (a)), relative to C_D at $\psi = 0°$, for $Re_w = 2.08 \times 10^6$. The change in C_D is presented along with corresponding change in the GTS mean base pressure coefficient ΔC_{p_b} (shown in subfigure (b)).

Figure 9 presents iso-surfaces of $\lambda_2 = -1500$ for the three yaw angles. Prior to the presence of crosswinds ($\psi = 0°$), the near-wake structure comprises two counter-rotating, longitudinal vortices (labelled A and B in figure 9). Higher strength associated with the upper shear layer (labelled A' in figure 9), *i.e* the shear layer proximate to the top surface of the GTS, relative to the lower one (labelled B' in figure 9), favors the interaction between the upper and both the side shear layers (labelled C' and D' in figure 9). The interaction results in the symmetric near-wake structure across the $Y^* = 0$ plane. Such changes in the near-wake structure at $\psi = 0°$ are beyond the focus of this study and therefore are not further discussed within this section, albeit $\psi = 0°$ cases are presented only for comparison to cases with the presence of crosswinds ($\psi \neq 0°$).

The veritable change in the near-wake structure, observed for $\psi = 8°$, relative to $\psi = 0°$, is a resultant of vortices C and D (labelled in figure 9), two streamwise, clockwise vortices emanating from the leeward and windward upper corners of the leading edge. The inclination of the flow relative to the front of the GTS results in the formation of the two vortices, in addition to vortex E (labelled in figure 9), emanating from the bottom, leeward corner of the leading edge and rotating counter-clockwise.

The effect of vortices C and D on the near-wake structure is clearly seen for $\psi = 8°$ and $10°$ (figure 9 (c)-(f)). Downstream of the GTS, *i.e.* in the near-wake region, the interaction between the tips of vortices C and D (labelled F and G in figure 9) and vortices A and B results in an abrupt reduction in the respective sizes of vortices A and B. The distinctive behavior of vortex D, relative to vortex C is a resultant of the direction of rotation of the interacting vortices. Here, the counter-clockwise rotation of vortices A, B and D results in the latter's abrupt change of direction in the near-wake. Such interaction results in the dampening of vortices A and B. It should be noted that the iso-surface value ($\lambda_2 = -1500$) was chosen to clearly highlight the variation in the vortical structure around the GTS, albeit using $\psi = 0°$ as a reference, the variation in the size of vortices A and B with an increasing ψ can be clearly interpreted in figure 9 (c)-(f).

The direction of vortices C and D can be attributed to the direction of crosswinds, albeit the effect on the direction of both the vortices varies, with vortex D displacing laterally onto the leeward side, while vortex C displaces vertically downwards. Such variation in the direction of both vortices can be attributed to the increase in their respective sizes, which varies proportionally with the crosswind magnitude. Here, the inclined flow ($\psi > 0°$) separates at the windward top edge of the GTS increasing the size of vortex D. The increase in the size of vortex C is a resultant of a similar mechanism at the leeward top edge. Flow visualization of the investigated yaw angles suggest the variation in the size to be linear, albeit further investigation is required to quantify such variation.

It should be noted that the size and direction of vortex E vary in a similar manner to vortices C and D, albeit flow visualization of all the investigated yaw angles conclude the vortex E to have minimal effect on the change in the near-wake structure. The minimal effect of vortex E is attributed to its change in direction relative to ψ. Here, an increase in the yaw angle displaces vortex E away from the GTS, minimizing its effect on the near-wake structure, as can be seen in figure 9 (d) and (f).

For $\psi = 15°$, the increase in the size of vortices C & D and the change in their respective direction results in their merge downstream onto one streamwise vortex (labelled H in figure 9 (e) and (f)). It is evident that the

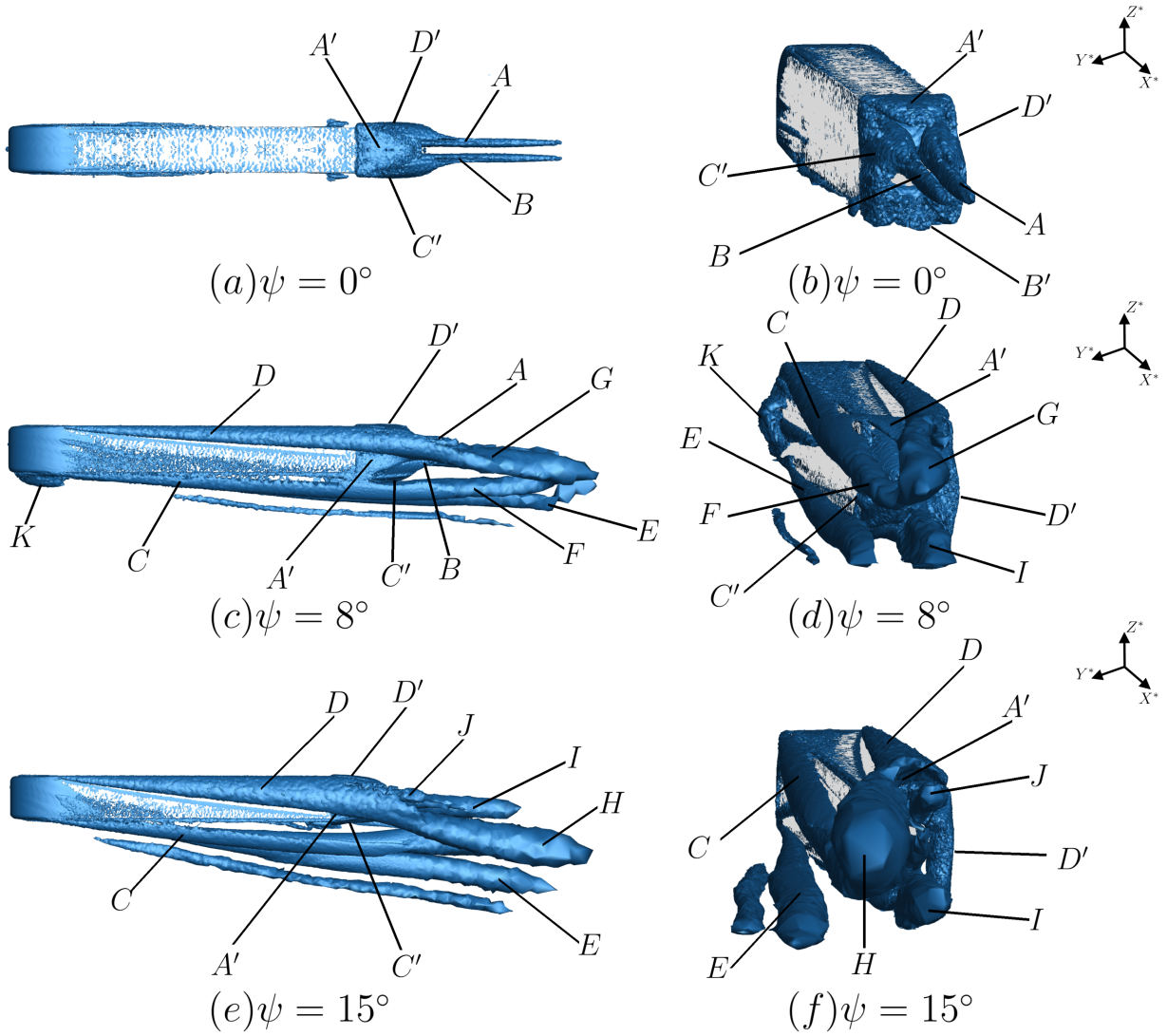

Figure 9: Visualization of $\lambda_2 = -1500$ iso-surfaces around the GTS at $Re_w = 2.08 \times 10^6$. In the top (left) and isomeric (right) planes, for $\psi = 0°$; (a) and (b), $\psi = 8°$; (c) and (d), and $\psi = 15°$; (e) and (f). A', B', C' and D' represent the upper, lower, leeward and windward shear layers, respectively. A and B are counter–rotating, streamwise vortices located in the near-wake region; C and D are co–rotating, streamwise vortices emanating from the leeward and windward corners of the leading edge for $\psi = 0°$; E is a streamwise vortex emanating from the bottom, corner of the leeward, leading edge; F and G are the tips of C and D; H is the resultant vortex of the merge of C and D; I and J are longitudinal vortices proximate to the lower and upper shear layers, and K is a separation bubble located at the leeward surface of the GTS. Note: Direction of crosswinds is top to bottom in (a), (c) and (e), while the flow direction is perpendicularly outward of the page in (b), (d) and (f).

emanation of vortex H results in a veritable change in the near-wake structure, relative to $\psi = 8°$. Its counter-clockwise rotation leads to an upward feeding motion, *i.e* vertical direction of the flow within the near-wake. Such upward feeding is not a resultant of a shear layer imbalance, as seen in laminar and turbulent Reynolds number cases presented in Badlani (2018) and Hassaan (2018), it is attributed to the direction of vortex H which aids in the upward feeding of the flow.

The lateral shift of vortex D onto the leeward side along with the introduced upward feeding mechanism leads to the emanation of two additional, counter-rotating vortices (labelled I and J in figure 9 (e) and (f)), quasi-parallel to the longitudinal axis of the GTS. Here, following the convention introduced in Badlani (2018) and Hassaan (2018), the *feeding vortex* is defined as the vortex from which the flow is fed, and *receiving vortex* is the vortex onto which the flow is fed. The flow from vortices I and H (feeding vortices in figure 9 (e) and (f)) is fed onto vortex J (receiving vortex in figure 9 (e) and (f)) resulting in the upward orientation of vortex J.

It should be noted that upon the induction of crosswinds, particularly within the yaw angle range; $2 < \psi° \leq 10$,

the inclination of the flow results in flow separation downstream of the leeward, leading edge of the GTS (labelled K in figure 9 (c) and (d)). The separation bubble is a resultant of an adverse pressure gradient downstream of the leading edge curvature. Boundary layer reattachment can additionally be observed upstream of the wake highlighting its minimal effect on the near-wake topology.

For yaw angles higher than 10°, particularly within the range; $10 < \psi^\circ \leq 15$, it is evident that vortex K (labelled in figure 9 (c) and (d)), located on the leeward side of the GTS, is not computed. The disappearance of vortex K is attributed to the downward displacement of vortex C, leading to the interaction between vortices C and K. Flow visualization of higher ψ (not shown here) concludes the interaction to be only within the range; $10 < \psi^\circ \leq 15$, attributed to the lateral shift of C away from K, albeit the change in the flow topology at $\psi > 15^\circ$ is beyond the scope of this study.

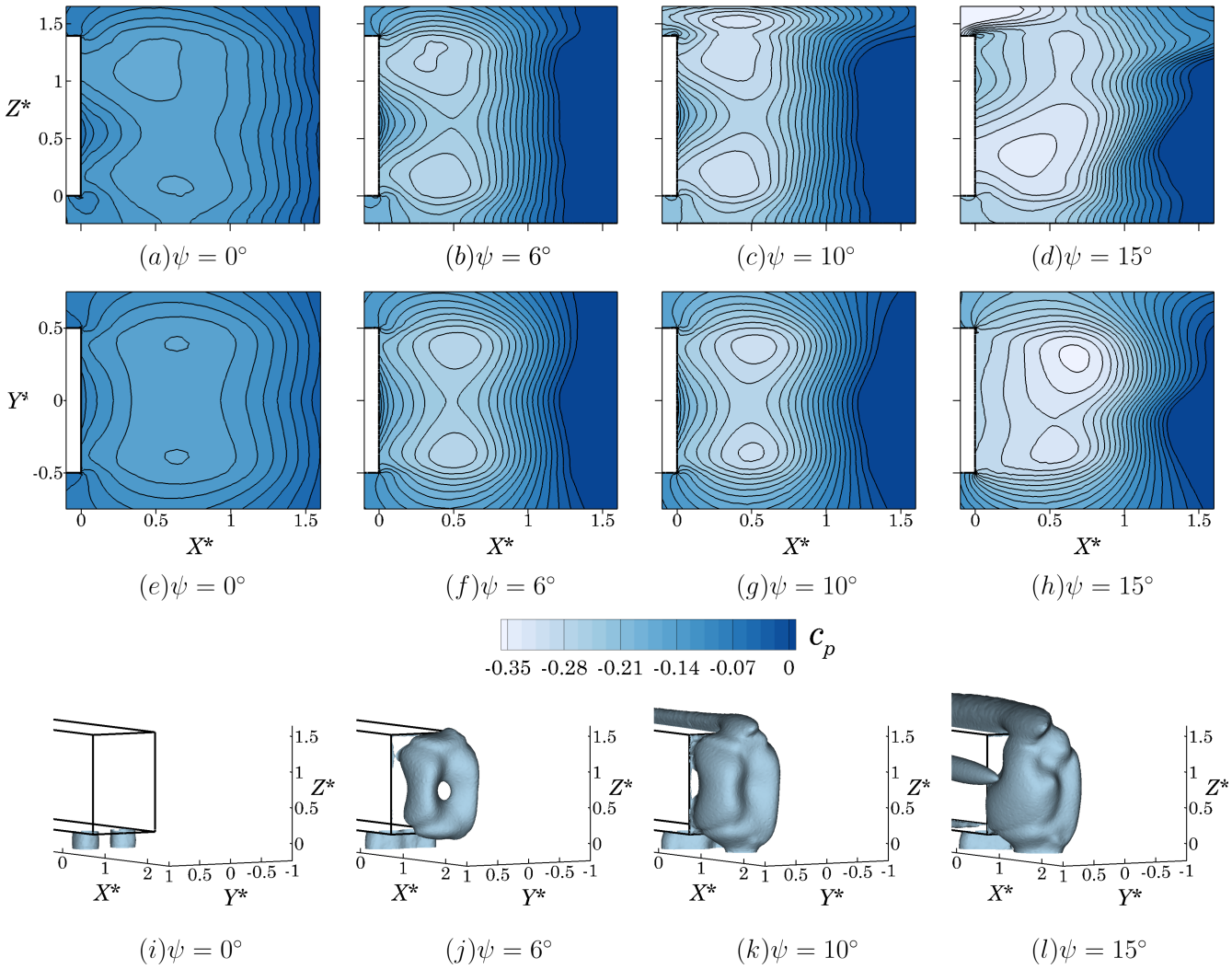

Figure 10: Visualization of static pressure coefficient (c_p) contours overlaid with bounding streamlines, at $Re_w = 2.08$ million, along the (a)–(d) $Y^* = 0$ plane and (e)–(h) the $Z^* = 0.7$ plane. For (a) and (e) $\psi = 0^\circ$, (b) and (f) $\psi = 6^\circ$, (c) and (g) $\psi = 10^\circ$ and (d) and (h) $\psi = 15^\circ$. Contours of (i)–(l) are iso-surfaces of $c_p = -0.25$, where (i) is $\psi = 0^\circ$, (j) is $\psi = 6^\circ$, (k) is $\psi = 10^\circ$, and (l) is $\psi = 15^\circ$. Contour levels are evenly spaced with $\Delta c_p = 0.07$.

Figure 10 $(a - h)$ show contours of the static pressure coefficient ($c_p = \dfrac{p_s - p_\infty}{q_\infty}$), where q_∞ is the freestream dynamic pressure. It can be seen that regions of low c_p bound the near-wake region, downstream of the GTS, within which regions of minimum c_p are collocated with the vortex cores along the planes; $Y^* = 0$ and $Z^* = 0.7$. Furthermore, a notable effect of ψ can be observed on the pressure within the near-wake region. Particularly for $\psi = 10^\circ$ and 15°, where an additional region of low c_p is observed, signifying the influence of the windward

stream-wise vortex (D) (see figure 9) on the pressure downstream of the simplified geometry. Such an effect can be further visualized by the three dimensional mapping of c_p presented in Figure 10 ($i - l$), within which iso-surfaces of $c_p < -0.2$ are shown. For $\psi = 10°$ and 15°, the emanation of vortex D results in a region of pressure minima collocated with its respective vortex core. For $\psi = 15°$, regions of minimal c_p are additionally observed, corresponding to the leeward, ground vortex (E). Furthermore, downstream of the near-wake region ($X^* \simeq 1$), an adverse pressure gradient is computed for all the yaw angles. Such an abrupt increase in c_p results in significant momentum losses downstream of the GTS, albeit no ground boundary layer separation was computed for all the investigated cases.

Figure 11 shows the variation of c_p along the $X^* = 0$ plane. Here, the effect of the near-wake pressure field is shown on the pressure variation along the base. For $\psi = 0°$, the symmetric flow topology is signified by the pressure variation along the plane, with the region of maximum c_p located along the $Y^* = 0$ line at $Z^* \simeq 0.5$. Furthermore, regions of minimal c_p are can be seen at $Z^* \simeq 0.25$ and $\simeq 1.1$, corresponding to the lower and upper low pressure regions in the near-wake (refer to figure 10). For $\psi = 6°$, the formation of vortex D (labelled in figure 11) resulted in the lateral shift of the stagnation point onto the leeward side of the simplified geometry. For $\psi = 10°$ the increased strength associated with vortices C and E (labelled in figure 11) leads to the displacement of the lower, c_p minima region onto the leeward side, subsequently increasing its overall size. The effect of vortices C and D is eminent for $\psi = 15°$. For $\psi = 15°$ the interaction between the bottom and windward, side shear layers results in an increase in the minima c_p bottom region, resulting in the upward shift of the stagnation point onto $Z^* \simeq 0.9$.

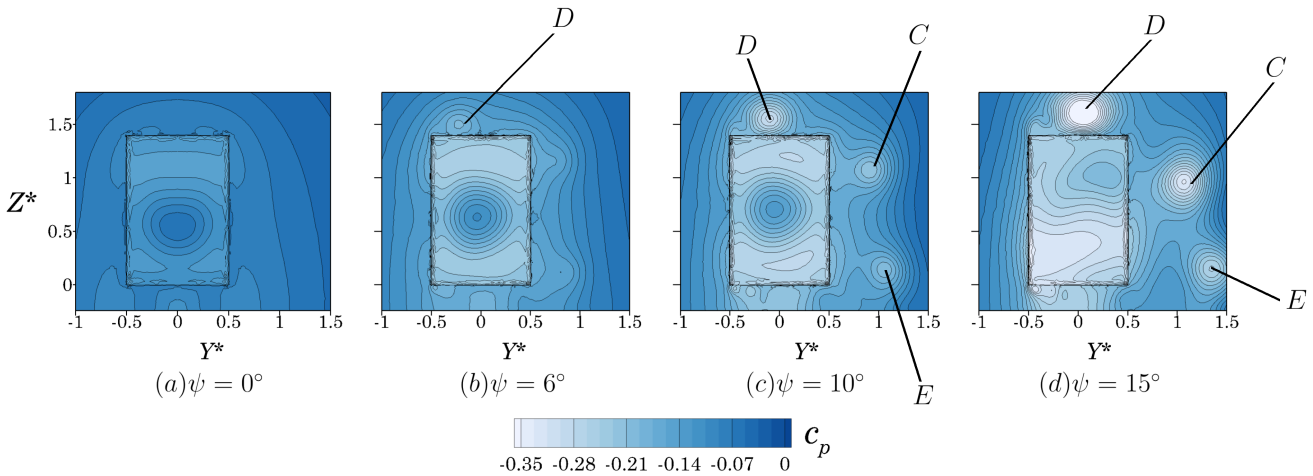

Figure 11: Visualization of static pressure coefficient (c_p) contours overlaid with bounding streamlines, at $Re_w = 2.08$ million, along the $X^* = 0$ plane (plane parallel to the rear-surface of the truck). Presented for; (a) $\psi = 0°$, (b) $\psi = 6°$, (c) $\psi = 10°$ and (d) $\psi = 15°$. The black box outlines the trailing edges of the GTS. Contour levels are evenly spaced with $\Delta c_p = 0.07$. Labels are consistent with figure 9. Note: Crosswind direction is from left to right.

4.1. Effect of boat-tail without presence of crosswinds

This section deals with investigating the effect of boat-tail addition on to the rear-end of the GTS at $\psi = 0°$ (no crosswinds). Four normalized boat-tail lengths (B^*), previously investigated by Burton et al. (2011), are considered. Boat-tail angles ranging from $0° \leq \beta \leq 25°$ were studied and compared for each of the four boat-tail lengths. Summary of the different configurations investigated within the present study are shown in table 1. Furthermore, critical cases are topologically compared to pinpoint changes befalling within proximity to the near-wake of the GTS.

Figure 12 shows variation of GTS drag coefficient (C_D) as a function of β for different boat-tail lengths. It is evident that at a constant β, an increase in B^* results in a reduction in C_D. Such reduction can be observed by comparing the shortest and longest boat-tail lengths ($B^* = 0.29$ and 0.74), where reduction in C_D ranges from $\sim 2\%$ at $\beta = 0°$ to $\sim 40\%$ at $\beta = 20°$.

Moreover, variation of C_D as a function of β for a constant B^* exhibits a sharp decrease in C_D within the range; $0° \leq \beta \leq 15°$, with the maximum reduction in C_D, equating to $\sim 45\%$, computed for $B^* = 0.74$ and $\beta = 15°$, respectively. At $15° < \beta < 20°$, a sharp increase in the aerodynamic drag is observed for all the cases except $B^* = 0.74$, showing the effect of boat-tail length on the shift of the critical boat-tail angle. For $\beta > 20°$, the drag

Table 1: Different boat-tail configurations investigated within the present study, where B^* represents the normalized boat-tail length (B/D_H), and β is the boat-tail slant angle.

B^*	$\beta°$
0.29	0, 12.5, 15, 20
0.44	0, 12.5, 15, 20, 25
0.6	0, 12.5, 15, 20, 25
0.74	0, 12.5, 15, 20, 25

coefficient almost equates to that of the baseline model making such geometric addition futile. Although, Burton et al. (2011) performed a study over an arbitrary heavy vehicle model with a streamlined front-end, the optimized boat-tail angle ($\beta = 15°$), *i.e.* boat-tail angle resulting in the lowest C_D, is consistent in both the studies.

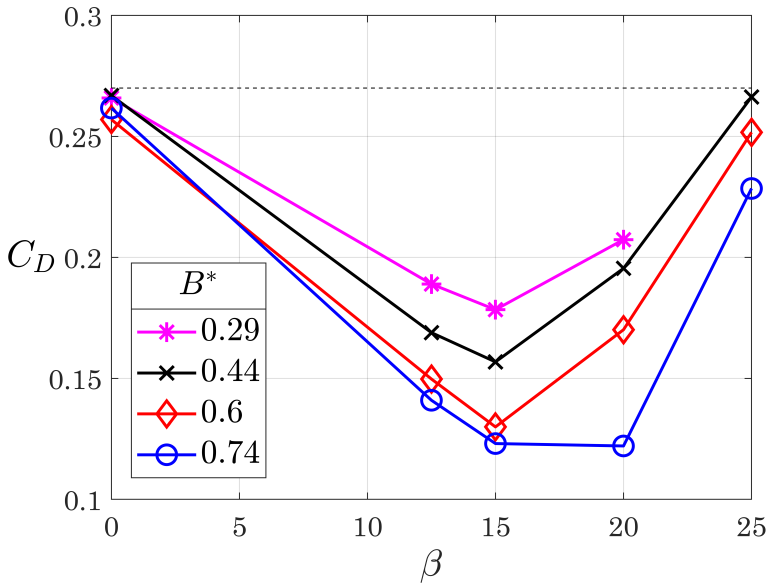

Figure 12: Variation of drag coefficient as a function of boat-tail angle β in degrees for different boat-tail lengths. Pink stars mark the $B^* = 0.29$ and the black cross and red diamonds plot the points for B^* of 0.44 and 0.6, respectively. Blue circles show the longest boat-tail length of $B^* = 0.74$. The horizontal, black dashed line represents the baseline GTS drag coefficient (without boat-tail).

Figure 13 shows the superimposed streamlines along with the velocity contours normalized with the free-stream velocity for the minimum and maximum boat-tail lengths considered in the course of this paper for $\beta = 12.5°, 15°$, and $20°$. For the case of $B^* = 0.29$, at $\beta = 12.5°$ (figure 13 (a)), flow consists of two counter-rotating vortices, with lower vortex of greater strength in comparison to the upper vortex due to a strong up-wash of flow emanating underneath the model. Saddle point is located at $[X^*, Z^*] = [1.5, 0.8]$ with upper vortex core at $[X^*, Z^*] = [0.9, 1.15]$. With increase in boat-tail angle to $\beta = 15°$, a restoration of symmetric wake is observed due to strong downwash of C–pillar vortices, emanating from the leading edge of boat-tail which acts as a C–pillar of the model, onto the stagnant flow in the wake. Similar downwash phenomenon was observed by Corallo et al. (2015) for Ahmed body at a slant angle of 25°. Saddle point has shifted vertically downward and upstream to $[X^*, Z^*] = [1.3, 0.69]$, with upper vortex core pulled closer to the base of the model aiding in a smaller wake size. Further increase in angle to $\beta = 20°$ shows a reduction in up-wash strength of the corner vortex, emanating from the bottom corners of GTS, with vanished lower vortex and upper vortex core shifted to, $[X^*, Z^*] = [0.2, 0.5]$, coupled with separated flow over lower boat-tail plate due to adverse pressure gradient leading to an enormous increase in wake size, decrease in wake pressure and high aerodynamic drag coefficient.

For $B^* = 0.74$, increased boat-tail length has broken the symmetric nature of the wake region. For $\beta = 12.5°$ (figure 13 (d)), flow consists of two similar to that of figure 13 (a) counter-rotating spanwise vortices with upper vortex in close proximity to aft end of upper boat-tail plate with its core at $[X^*, Z^*] = [1.1, 1]$ and saddle point at $[X^*, Z^*] = [1.6, 0.56]$. Upper vortex formation is due to the integration of upper shear layer with the wake flow and this feeds into the lower vortex which lies at $[X^*, Z^*] = [0.4, 0.7]$. Increase in boat-tail angle to $\beta = 15°$ (figure 13 (e)) shows complete disappearance of lower vortex with upper vortex core lying at the location of $[X^*, Z^*] = [0.4, 0.7]$.

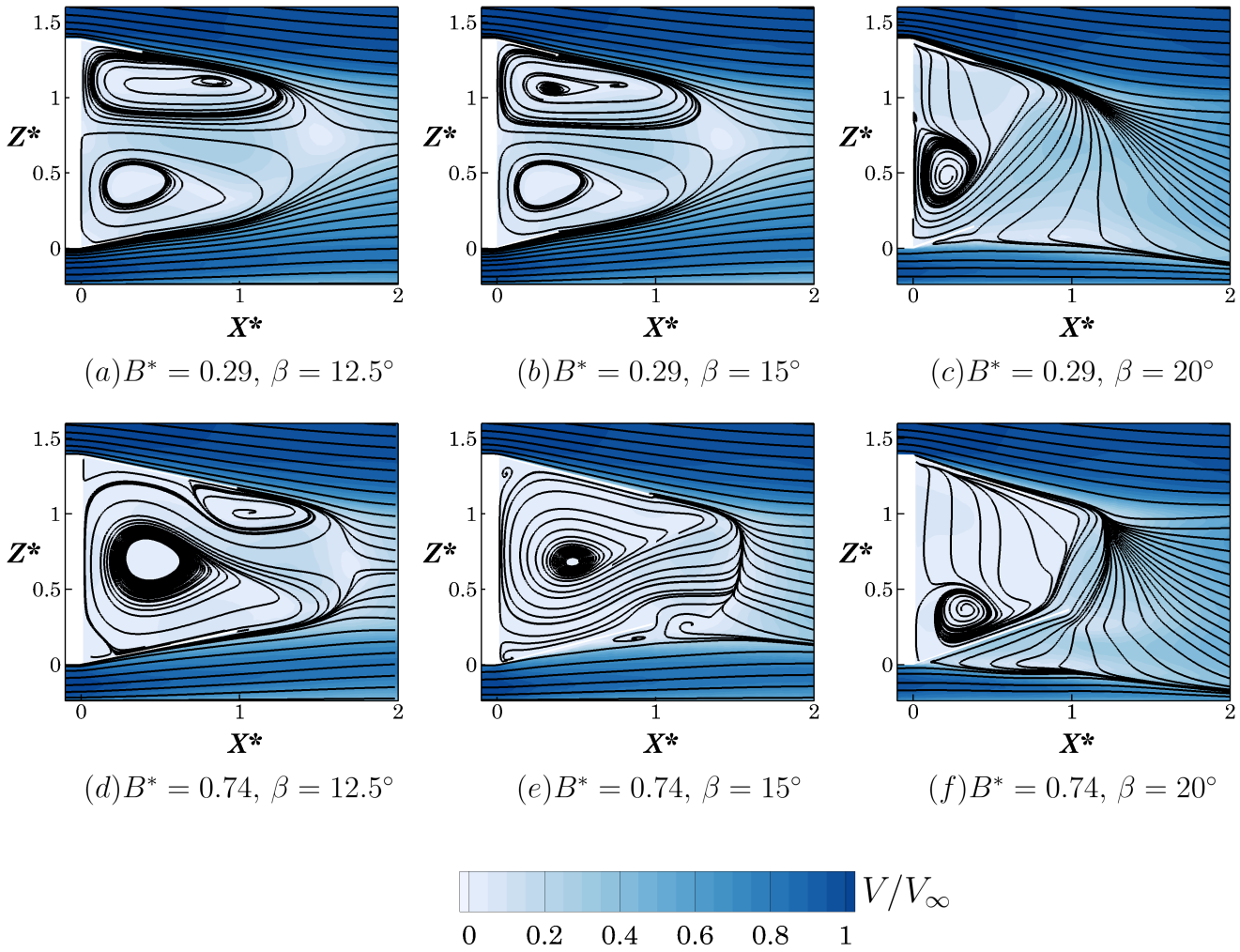

Figure 13: Velocity field contours overlaid with streamlines at the $Y^* = 0$ symmetry plane for different configurations of the boat-tail attached. (a)–(c) show the streamlines in the wake region for the shortest boat-tail ($B^* = 0.29$) and for boat-tail angles of $\beta = 12.5°, 15°$ and $20°$, respectively. (d)–(f) show the streamlines overlaid for the longest boat-tail configuration ($B^* = 0.74$) at boat-tail angles of $\beta = 12.5°, 15°$ and $20°$, respectively. Contour levels are evenly spaced with $\Delta V/V_\infty = 0.2$.

It is worthwhile to notice that, lower vortex vanished at a lower boat-tail angle for the longer configuration in comparison to $B^* = 0.29$ which occurred at $\beta = 20°$. This can be attributed to strong downwash of the C–pillar vortex also feeding into lower boat-tail plate causing slight separation of flow towards the end of the boat-tail span. Further increasing the angle to $\beta = 20°$, shows a strengthened downwash of C–pillar vortices promoting highly attached flow initially followed by a bouncing of the flow away from the upper boat-tail plate in the symmetry plane with strong feed into the boat-tail cavity, shifting the spanwise vortex core to $[X^*, Z^*] = [0.27, 0.37]$ with upstream shift of lower boat-tail flow separation. In the last two cases, reduced wake size coupled with increased pressure has led to reduction in overall drag with a maximum drag reduction of 54.1% lower than that of the baseline model.

Figure 14, shows distribution of coefficient of pressure in the near-wake of the GTS for different boat-tail angles of $\beta = 12.5°, 20°$ and, $25°$ at $B^* = 0.74$. It is evident that for boat-tail slant angles higher than the optimized case, *i.e.* $\beta = 20°$, a significant reduction in c_p can be observed. Therefore, it becomes important to further identify the cause of reduction in the coefficient of pressure amidst the $\beta = 20°$ and $\beta = 25°$ models which lead to approximately 46% variation in the aerodynamic drag coefficient.

Figure 15 shows pressure coefficient contours in the near-wake of GTS. It is evident that, for $\beta = 20°$, flow remains attached for longer time at the upper half of boat-tail in comparison to $25°$ case. In the lower half, highly stagnant vortex observed in $\beta = 25°$ model has been eradicated for $\beta = 20°$ and instead a smooth flow from upper end feeds into the lower half of boat-tail due to which a relatively higher-pressure region has been created in the

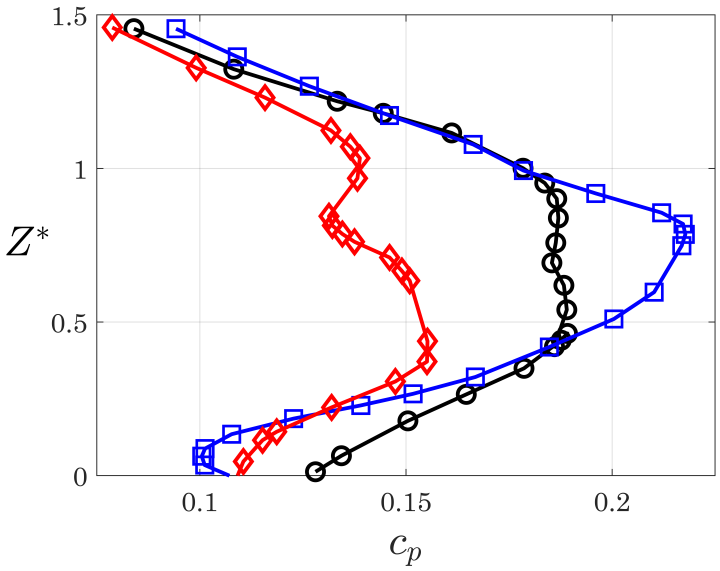

Figure 14: Vertical distribution of the coefficient of pressure (c_p) in the near-wake of the GTS equipped with a boat-tail of with $B^* = 0.74$. Presented at $X^* = 1.684$ along the symmetry plane, for; $\beta = 12.5°$ (black colored hollow circles), $\beta = 20°$ (blue colored squares) and $\beta = 25°$ (red colored diamonds).

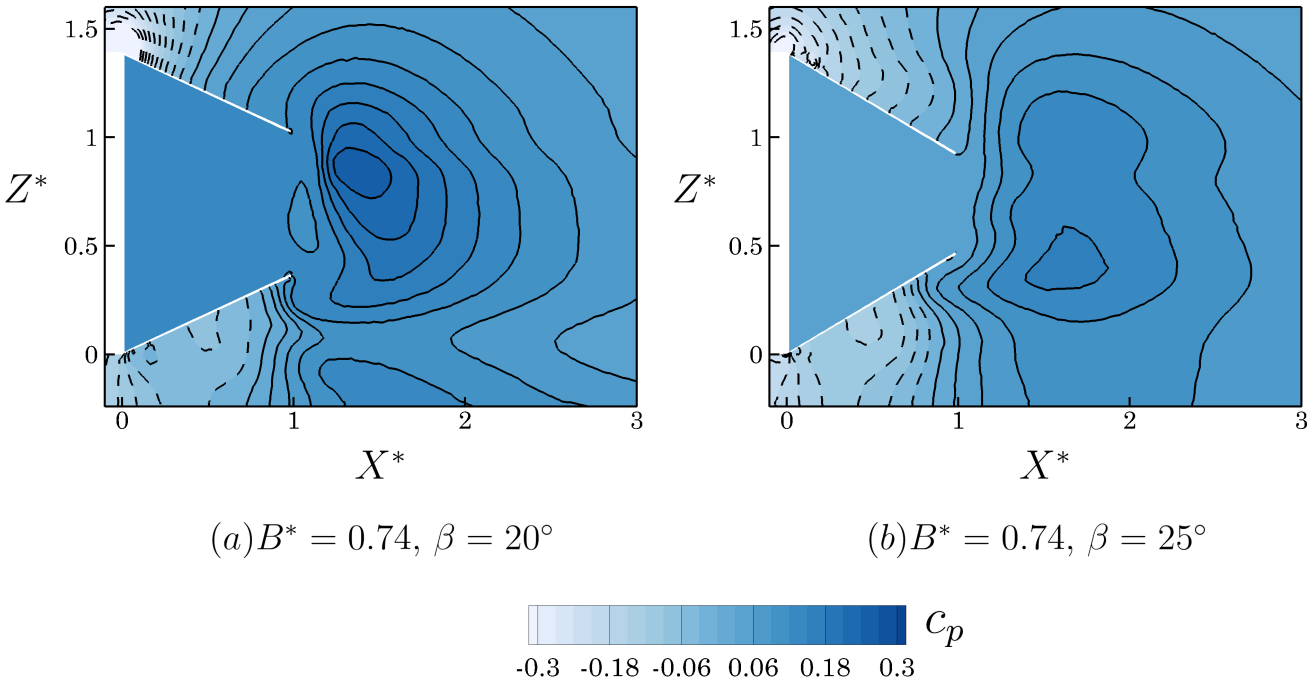

Figure 15: Contours of the static pressure coefficient (c_p) in the wake region for (a) $B^* = 0.74$, $\beta = 20°$ and (b) $B^* = 0.74$, $\beta = 25°$. Solid and dashed lines represent positive and negative values of c_p, respectively. Contour levels are evenly spaced with $\Delta c_p = 0.12$.

wake. A shift in the wake topology can be visualized with upper vortex core computed at $[X^*, Z^*] = [0.28, 0.9]$ for $\beta = 25°$ to $[X^*, Z^*] = [0.36, 0.38]$ for $\beta = 20°$. An additional spanwise vortex formed at $[X^*, Z^*] = [1.05, 0.8]$ coupled with flow separation over the upper boat-tail plate for the $\beta = 25°$ model is responsible for a topological change in the wake region. Therefore, due to the high pressure in the wake region coupled with increased C–pillar down-wash strength for 20° boat-tail configuration in comparison to larger low-pressure area and reduced C–pillar down-wash strength in the wake of 25° boat-tail configuration, the overall pressure difference at the frontal and rear end of GTS model has reduced. This yields in a 54.1% drag reduction from the baseline model with the least

drag coefficient value of 0.1221 for 20° perusal.

Figure 16 shows the iso-surface of the λ_2 criterion ($\lambda_2 = -5000$) for the simplified heavy vehicle with boat-tail plates at angles of $\beta = 12.5°, 15°$ and 20° for the maximum and minimum lengths of boat-tail configuration considered. These demonstrate a substantial activity of vortices generated at the frontal and near-wake regions of the heavy vehicle. Two pairs of counter-rotating, and longitudinal vortices emanate from the frontal curvatures of the top and bottom surface of the GTS model. Slight frontal separation with quick reattachment of the flow is visible at the sides of the frontal end from whereon the flow stays completely attached to the model until it reaches the leading edge of the boat-tail where the flow separates once again followed by a quick reattachment onto the boat-tail surface. Across the highly contrasting drag coefficient of various configurations, these frontal end vortical structures is similar in all the cases. For $B^* = 0.29$, and $\beta \leq 15°$, the flow stays attached to the surface of the boat-tail with a quasi-symmetric topology of the wake region consisting of a pair of spanwise counter-rotating vortices. The disturbed symmetric nature of the flow with increasing angle of boat-tail and strengthened C–pillar downwash steered the downstream extension of the longitudinal vortical structure with some part of its strength feeding into the boat-tail cavity. Bottom and side shear layer interaction with adverse pressure gradient at the lower boat-tail led to the upwash of the flow emanating from the bottom of the model as corner vortices, which extend far downstream. For the longer boat-tail configuration, at $\beta = 12.5°$, the upwash from the corner vortices is weaker in comparison to the $\beta \geq 15°$ configuration. This is due to the presence of strong downwash from the C–pillar vortices and injection of flow into the boat-tail cavity and lower boat-tail boundary layer separation. The strength of the two pairs of longitudinal vortices at $\beta \geq 15°$ is derived from the disappearance of lower spanwise vortex which feeds into the longitudinal vortices increasing their strength and extension further downstream. These findings are in agreement with Corallo et al. (2015), who observed a similar kind of feeding mechanism at $AR = 0.9$ and slant angle of 25°.

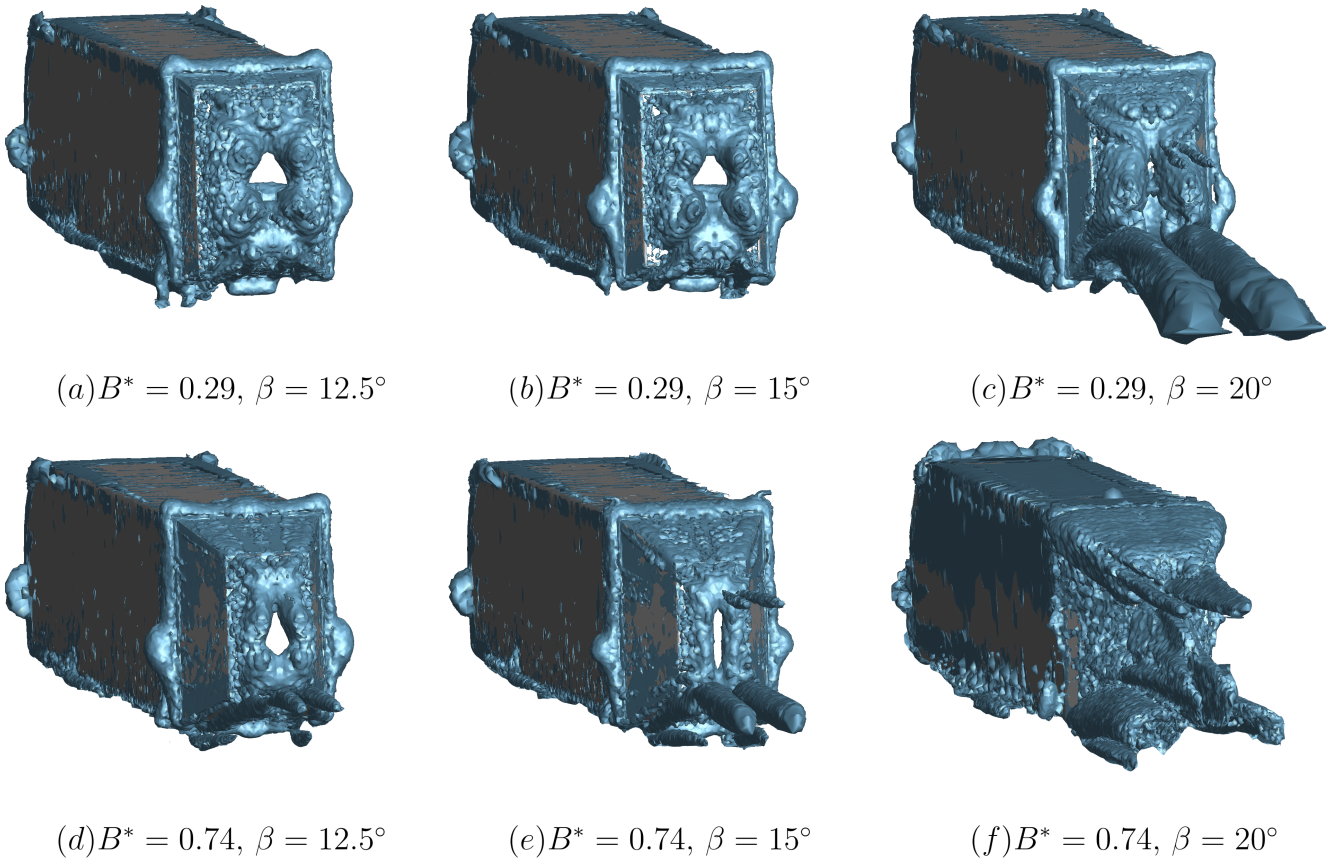

$(a) B^* = 0.29,\ \beta = 12.5°$ $(b) B^* = 0.29,\ \beta = 15°$ $(c) B^* = 0.29,\ \beta = 20°$

$(d) B^* = 0.74,\ \beta = 12.5°$ $(e) B^* = 0.74,\ \beta = 15°$ $(f) B^* = 0.74,\ \beta = 20°$

Figure 16: Iso-surface visualization for the λ_2 criterion ($\lambda_2 = -5000$) shown for (a)–(c) $B^* = 0.29$ and $\beta = 12.5°, 15°$ and 20°, respectively and for (d)–(f) $B^* = 0.74$ and $\beta = 12.5°, 15°$ and 20°, respectively

4.2. Effect of boat-tail with crosswinds

In section 4.1, the effect of varying the boat-tail length (B^*) and slant angle (β) was investigated on the GTS drag coefficient and near-wake structure without the presence of crosswinds ($\psi = 0°$). In the following section, the effect of varying β on the drag coefficient of the GTS and the corresponding near-wake structure are reported for various yaw angles. Up to the authors' best of knowledge, the effect of a boat-tail on the near-wake structure, with the presence of crosswinds, was not previously reported within the literature. The study was conducted on a boat-tail with a normalized length (B^*) of 0.44, for three boat-tail angles (β); 12.5°, 15° and 20°.

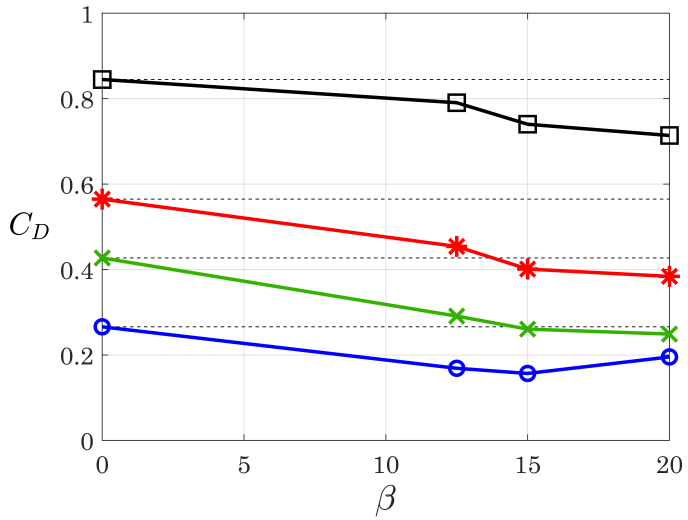

Figure 17: Variation of the coefficient of drag (C_D) with boat-tail angle (β) in degrees, where $\beta = 0°$ corresponds to the baseline GTS (without boat-tail) at yaw angles of $\psi = 0°$ (blue hollow circles), $\psi = 6°$ (green $\times$ markers), $\psi = 10°$ (red stars) and $\psi = 15°$ (black hollow squares).

Figure 17 presents the variation of the GTS (with boat-tail) drag coefficient (C_D) with $\beta°$ for $\psi = 0°$, 6°, 10° and 15°, respectively. $\beta = 0°$ represents baseline GTS drag coefficient, *i.e.* prior to the attachment of the boat-tail. As previously discussed in section 4.1, without the presence of crosswinds, the boat-tail slant angle corresponding to maximum reduction in C_D equates to 15°. Higher boat-tail slant angles result in a rise in the C_D. On the contrary, with the presence of crosswinds, slant angles higher than 15° result in further reduction in C_D, albeit at a lower rate relative to $\beta < 15°$. Furthermore, comparing the variation in C_D for $\psi = 6°$ and $\psi = 10°$ suggests the reduction in C_D obtained from slant angles higher than 15° to increase proportionally with ψ. However further investigations are required to quantify such a hypothesis.

Figure 18 shows contours of normalized velocity magnitude ($\sqrt{u_i + u_j}/V_\infty$), overlaid with streamlines in the near-wake of the GTS along the $Z^* = 0.7$ plane, for $\psi = 0°$, 10° and 15° and for $\beta = 0°$, 15° and 20°. For $\psi = 0°$, the reduction in drag associated with $\beta = 15°$ is a resultant of the reduction in the size of the wake, equating to $\simeq 27\%$ smaller wake length (l_w), defined as the distance between the saddle point and the base of the GTS. The abrupt increase in drag found for $\beta = 20°$ is a resultant of flow detachment from the boat-tail surface (not visible in the plane). For $\psi = 10°$ and 15°, the asymmetric, near-wake structure downstream of the baseline model is a resultant of vortices C, D and E (see figure 9). Along the $Z^* = 0.7$ plane, lateral feeding from vortices C and E results in the asymmetric near-wake structure, signified by the increase of the leeward vortex size relative to the windward one. The asymmetric near-wake structure results in an abrupt reduction in the mean base pressure and leads to the higher C_D. As β increases further, *i.e.* $\beta = 15°$ and 20°, the upper and leeward boat-tail plates prevent the interaction between vortices C, D and E (labelled in figure 9) and the side and upper shear layers. Henceforth, aiding in the restoration of symmetry within the near-wake region.

Figure 19 shows iso-surfaces of the $\lambda_2 = -5000$ criterion for $\psi = 0°$, 10° and 15°, for the boat-tail models of $\beta = 15°$ and 20°. For $\psi = 0°$, the abrupt rise in C_D, between $\beta = 15°$ and 20°, is a resultant of the formation of two C–pillar vortices, *i.e.* two vortices parallel to a slanted surface, from the bottom two corners of the base. Such vortices highlight the complete detachment of the flow from the surface of the boat-tail, consequently increasing the vertical size of the wake. For $\psi = 10°$, downstream of the GTS, the downward shift of the windward, streamwise vortex distrupts the development of the C–pillar vortex on the leeward side. Furthermore, for $\beta = 20°$ the lateral feeding associated with the leeward streamwise vortex aids in the attachment of flow onto the leeward boat-tail

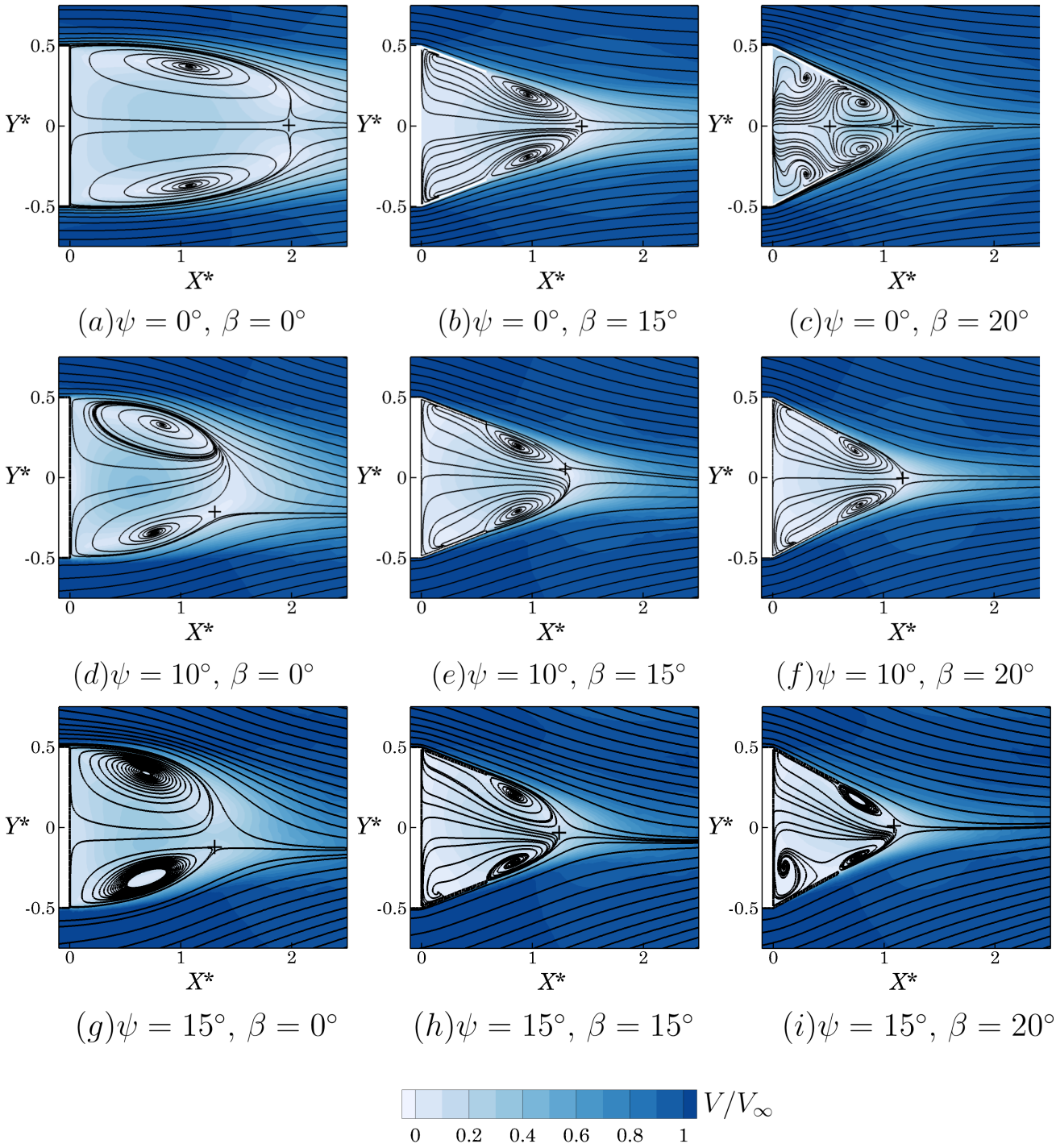

Figure 18: Normalized velocity magnitude ($\sqrt{u_i + u_j}/V_\infty$) contours along the $Z^* = 0.7$ plane, for (a)–(c) $\psi = 0°$; (d)–(f) $\psi = 10°$; and (g)–(i) $\psi = 15°$. (a), (d) and (g) are for baseline GTS, (b), (e) and (h) $\beta = 15°$ and (c), (f) and (i) $\beta = 20°$. Crosses are locations of saddle points. Contour levels are evenly spaced with $\Delta V/V_\infty = 0.2$. Note: Crosswind direction is bottom to top.

plate, albeit separation along the lower and windward plates is observed. It can be seen that a similar vortical structure is computed for the $\psi = 15°$ cases, relative to $\psi = 10°$. With exception to the size of the vortices, which were discussed earlier within section 4.

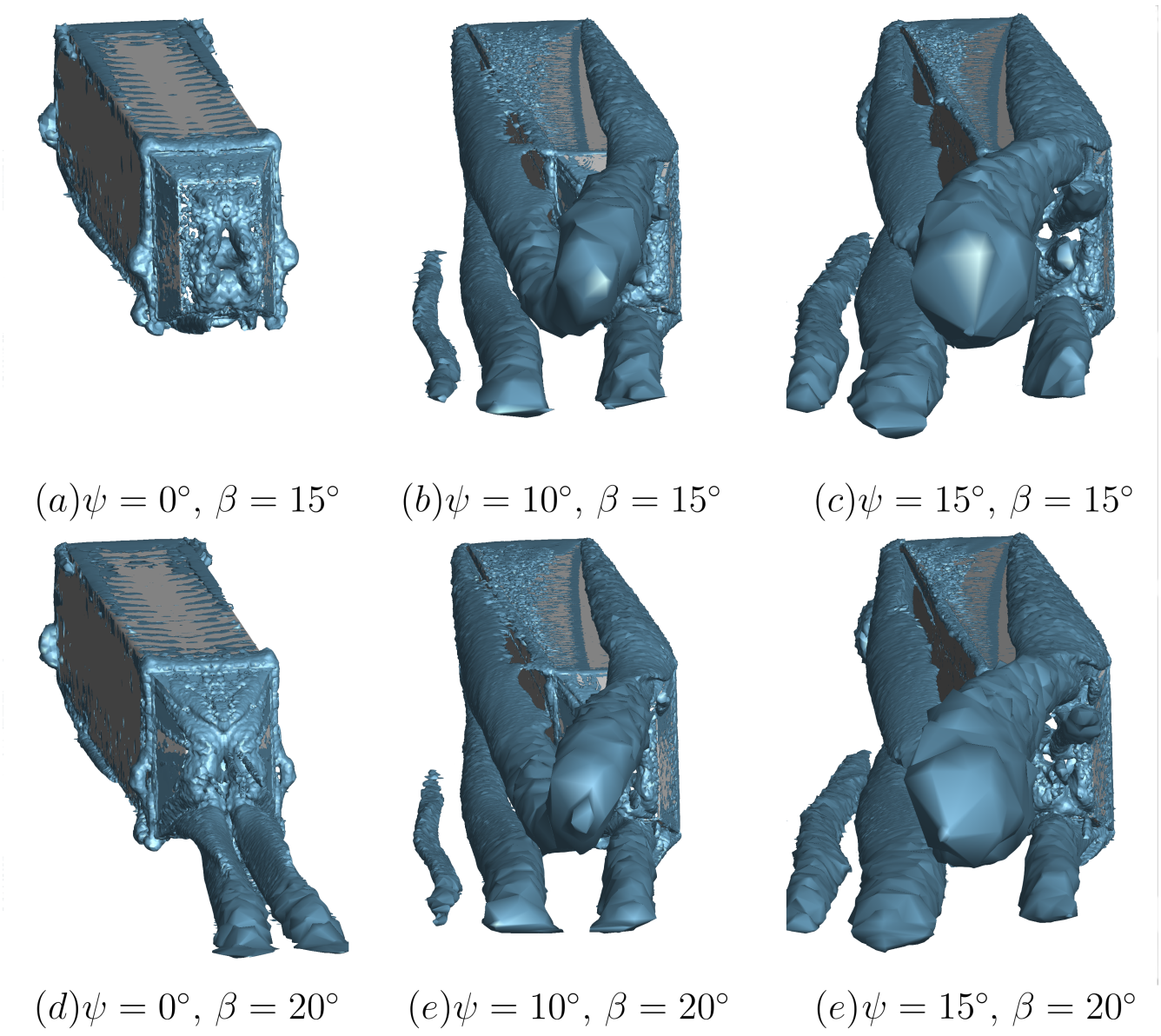

Figure 19: Iso-surfaces of $\lambda_2 = -5000$ around the GTS with boat-tail for $\psi = 0°$: (a) $\beta = 15°$ and (d) $\beta = 20°$; $\psi = 10°$: (b) $\beta = 15°$ and (e) $\beta = 20°$; and $\psi = 15°$: (c) $\beta = 15°$ and (e) $\beta = 20°$. Note: Crosswind direction is from right to left.

5. Conclusion

The flow around a 1 : 8 scaled, Ground Transportation System (GTS), was numerically investigated using the steady formulation of the RANS, $k-\omega$ Shear Stress Transport (SST) model, at a Reynolds number of ~ 2 million. Upon the emanation of crosswinds, a significant change in the overall flow structure around the GTS was observed. Such variation is characterized by three, streamwise vortices, forming at the leading edges of the GTS. Visualization of the near-wake region show the three streamwise vortices to develop onto the near-wake region, where interaction between the three vortices and the near-wake results in a notable change in the latter's structure. Such change in the near-wake structure has resulted in a quadratic decrease in the mean base pressure of the GTS, as a function of the yaw angle (ψ) and the corresponding quadratic increase in the GTS drag coefficient (C_D).

The addition of boat-tail onto the rear-end of the GTS, in both cases with and without crosswinds, have resulted in a significant reduction in the size of the near-wake. For cases without crosswinds, the addition of a boat-tail has resulted in up to $\sim 50\%$ reduction in C_D relative to the baseline GTS (without boat-tail). Here, for all the investigated boat-tail lengths, highest drag reduction was observed for a boat-tail slant angle (β) of 15°. An abrupt rise in C_D was also observed for boat-tail slant angles higher than 15°. This finding is consistent with previous

studies of Yi et al. (2007) and Burton et al. (2011), who investigated the effect of a boat-tail slant angle on the drag coefficient of various simplified geometries. An exception to such a finding was observed for the highest boat-tail length ($B^* = 0.74$), where quasi-constant variation in C_D was observed between $\beta = 15°$ and $20°$. For cases with crosswinds, drag reduction of up to $\sim 40°$, relative to the baseline GTS, was found for higher boat-tail slant angles. The significant drag reduction is attributed to the restoration in the quasi-symmetry of the near-wake, typically observed on bluff bodies for $\psi = 0°$, upon the addition of the boat-tail at various slant angles. Here, the boat-tail acts as a blockage, preventing the interaction between the three streamwise vortices (shedding from the frontal corners of the GTS) and the near-wake.

Funding

This research did not receive any specific grant from funding agencies in the public, commercial, or not-for-profit sectors.

Nomenclature

A_c	Cross-sectional area
B	Boat-tail length
C_D	Coefficient of drag
CFD	Computational Fluid Dynamics
C_{p_b}	Mean base pressure coefficient
D	Diameter of the cylindrical struts
D_H	Hydrualic diameter
G	Height of the GTS from the ground
GTS	Ground Transportation System
k	Turbulent kinetic energy
L	Length of the GTS
l_w	Streamwise length of the wake
n_{cell}	Number of mesh cells
PIV	Particle Image Velocimetry
RANS	Reynolds Averaged Navier Stokes
Re_w	Reynolds number based on the width of the GTS
SST	Shear Stress Transport
u	Velocity
V	Velocity Magnitude
w	Width of the GTS
α	Boat-tail slant angle in figure 1 (Yi et al., 2007)
β	Boat-tail slant angle
ϵ	Turbulent dissipation rate
ω	Specific turbulent dissipation rate
ψ	Yaw angle

Subscripts.

∞	Freestream quantity
x	Streamwise quantity
y	Spanwise quantity
z	Vertical quantity

Superscripts.

$*$	Normalized by the width of the GTS with the exception of B^* (normalized by D_H)
$\bar{i}$	Mean value of i, where i is an arbitrary variable

References

Alonso-Estébanez, A., Díaz, J. D. C., Rabanal, F. Á., Pascual-Muñoz, P., 2017. Performance analysis of wind fence models when used for truck protection under crosswind through numerical modeling. Journal of Wind Engineering

and Industrial Aerodynamics 168, 20–31.
doi: https://doi.org/10.1016/j.jweia.2017.04.021

Badlani, D., April 2018. Effect of geometric modifications on the near wake flow topology of a simplified heavy vehicle. Final year project, Heriot–Watt University.

Burton, D., Nazarinia, M., Sheridan, J., Parkin, D., 2011. Optimisation of boat-tails for heavy vehicles. In: ASME-JSME-KSME 2011 Joint Fluids Engineering Conference. American Society of Mechanical Engineers, pp. 885–891.
doi: https://doi.org/10.1115/AJK2011-23009

Cheli, F., Belforte, P., Melzi, S., Sabbioni, E., Tomasini, G., 2006. Numerical–experimental approach for evaluating cross-wind aerodynamic effects on heavy vehicles. Vehicle System Dynamics 44, 791–804.
doi: https://doi.org/10.1080/00423110600886689

Choi, H., Lee, J., Park, H., 2014. Aerodynamics of heavy vehicles. Annual Review of Fluid Mechanics 46, 441–468.
doi: https://doi.org/10.1146/annurev-fluid-011212-140616

Coon, J., Visser, K., 2004. Drag reduction of a tractor-trailer using planar boat tail plates. In: The Aerodynamics of Heavy Vehicles: Trucks, Buses, and Trains. Springer, pp. 249–265.

Cooper, K. R., 1985. The effect of front-edge rounding and rear-edge shaping on the aerodynamic drag of bluff vehicles in ground proximity. SAE Transactions, 727–757.

Corallo, M., Sheridan, J., Thompson, M., 2015. Effect of aspect ratio on the near-wake flow structure of an Ahmed body. Journal of Wind Engineering and Industrial Aerodynamics 147, 95–103.
doi: https://doi.org/10.1016/j.jweia.2015.09.006

Croll, R., Gutierrez, W., Hassan, B., Suazo, J., Riggins, A., 1995. Experimental investigation of the ground transportation systems (GTS) project for heavy vehicle drag reduction.

Good, G. M. L., Garry, K. P., 2004. On the use of reference models in automotive aerodynamics. In: SAE Technical Paper. SAE International.
doi: https://doi.org/10.4271/2004-01-1308

Grandemange, M., Gohlke, M., Cadot, O., 2013. Turbulent wake past a three-dimensional blunt body. part 1. global modes and bi-stability. Journal of Fluid Mechanics 722, 51–84.
doi: https://doi.org/10.1017/jfm.2013.83

Gutierrez, W., Hassan, B., Croll, R., Rutledge, W., 1996. Aerodynamics overview of the ground transportation system (GTS) project for heavy vehicle drag reduction. SAE 960906, 219–236.
doi: https://doi.org/10.4271/960906

Hassaan, M., April 2018. Numerical study on the effect of upstream conditions on the near–wake flow topology of a simplified heavy vehicle. Final year project, Heriot–Watt University.

Howell, J., Sheppard, A., Blakemore, A., 2003. Aerodynamic drag reduction for a simple bluff body using base bleed. In: SAE Technical Paper. SAE International.
doi: https://doi.org/10.4271/2003-01-0995

Hucho, W.-h., Sovran, G., 1993. Aerodynamics of road vehicles. Annual review of fluid mechanics 25 (1), 485–537.
doi: https://doi.org/10.1146/annurev.fl.25.010193.002413

Jeong, J., Hussain, F., 1995. On the identification of a vortex. Journal of Fluid Mechanics 285, 69–94.
doi: https://doi.org/10.1017/S0022112095000462

Lögdberg, O., 2008. Turbulent boundary layer separation and control. Ph.D. thesis, KTH.

Maddox, S., Squires, K. D., Wurtzler, K. E., Forsythe, J. R., 2004. Detached–eddy simulation of the ground transportation system. In: The Aerodynamics of Heavy Vehicles: Trucks, Buses, and Trains. Springer, pp. 89–104.
doi: https://doi.org/10.1007/978-3-540-44419-0_8

McArthur, D., Burton, D., Thompson, M., Sheridan, J., 2016. On the near wake of a simplified heavy vehicle. Journal of Fluids and Structures 66, 293–314.
doi: https://doi.org/10.1016/j.jfluidstructs.2016.07.011

McArthur, D., Burton, D., Thompson, M., Sheridan, J., 2018. An experimental characterisation of the wake of a detailed heavy vehicle in cross-wind. Journal of Wind Engineering and Industrial Aerodynamics 175, 364 – 375.
doi: https://doi.org/10.1016/j.jweia.2018.01.033

McCallen, R., Couch, R., Hsu, J., Browand, F., Hammache, M., Leonard, A., Brady, M., Salari, K., Rutledge, W., Ross, J., Storms, B., Heineck, J., Driver, D., Bell, J., Zilliac, G., 1999. Progress in reducing aerodynamic drag for higher efficiency of heavy duty trucks (class 7-8).
doi: 10.4271/1999-01-2238

Menter, F. R., 1994. Two-equation eddy-viscosity turbulence models for engineering applications. AIAA journal 32 (8), 1598–1605.
doi: https://doi.org/10.2514/3.12149

Rao, A., Minelli, G., Basara, B., Krajnović, S., 2018. On the two flow states in the wake of a hatchback ahmed body. Journal of Wind Engineering and Industrial Aerodynamics 173, 262–278.
doi: https://doi.org/10.1016/j.jweia.2017.10.021

Roy, C. J., Ghuge, H. A., 2009. Detached–eddy simulations of a simplified tractor/trailer geometry. In: The Aerodynamics of Heavy Vehicles II: Trucks, Buses, and Trains. Springer, pp. 363–381.
doi: https://doi.org/10.1007/978-3-540-85070-0_34

Salari, K., Ortega, J., Castellucci, P., 2004. Computational prediction of aerodynamic forces for a simplified integrated tractor-trailer geometry. AIAA 2004-2253. In: 34^{th} AIAA Fluid Dynamics Conference.
doi: https://doi.org/10.2514/6.2004-2253

Söderblom, D., Elofsson, P., Hjelm, L., Löfdahl, L., 2016. Wheel housing aerodynamics on heavy trucks. In: The Aerodynamics of Heavy Vehicles III. Springer, pp. 211–223.
doi: https://doi.org/10.1007/978-3-319-20122-1_13

Storms, B. L., Ross, J. C., Heineck, J. T., Walker, S. M., Driver, D. M., Zilliac, G. G., Bencze, D. P., 2001. An experimental study of the ground transportation system (GTS) model in the NASA Ames 7-by 10-ft wind tunnel. Technical Report NASA/TM-2001-209621, NASA.

Van Raemdonck, G. M. R., 2012. Design of low drag bluff road vehicles. PhD Thesis of Delft University of Technology.

Wood, R. M., 2006. A discussion of a heavy truck advanced aerodynamic trailer system. In: Int. Symp. Heavy Veh. Weights Dimens., 9th, University Park, PA.

Yi, W., SaGong, W., Choi, H.-C., 2007. Drag reduction of a three-dimensional car model using passive control device. In: Proceedings of the KSME Conference. The Korean Society of Mechanical Engineers.